Field data example

The results thus far have been created using synthetically generated data. Whilst this is a useful exercise to validate and test concepts, it is necessary to demonstrate how this approach works on a 3D field data set. Field data features a range of attributes that were missing from these synthetic data, including converted waves, incoherent noise, coherent noise, processing artifacts, irregular sampling of receiver and source points, anisotropy, attenuation, and more. Each of these will pose new challenges for the process of inverse Born modeling, and the procedure must be robust enough to handle these real-world imperfections.

THE DATASET

The dataset used was acquired using Ocean Bottom Node (OBN) acquisition, will a total of 1195 receivers. Each receiver had a maximum offset (source position range) of 20 km in both inline and crossline directions, and the time sampling was 4 ms. The full imaging cube was 30 km x 30 km x 18 km, although for the purpose of demonstrating image-based shot separation, a smaller section was windowed.

An area of 20 km x 20 km x 8 km was targeted for imaging, using 103 receivers, which featured a concurrent shooting pattern. From the principal of reciprocity, these can be considered as 103 shot gathers. Initially, RTM and linearized inversion were applied to these gathers. The benefits of this were twofold: the concept of LSRTM could be tested on field data, and a reference image to compare post-separation results and be created. The nature of both the Earth models provided and the acquisition necessitated several changes to the imaging approach from the last three chapters.

Firstly, the survey area featured a variety of dips, salt bodies, and subsurface stress states. This meant that earlier efforts at imaging the target described the subsurface as a Tilted Transverse Isotropic (TTI) medium (**?**). The previous chapters stated that the subsurface could be described using a velocity field, $\mathbf{v}(x, y, z)$, which could be split into high-wavenumber and low-wavenumber components. This assumed an acoustic, isotropic subsurface (discussed in Chapter 2.) For a TTI medium, four additional parameter fields (as well as velocity) are needed to simulate wave propagation and perform imaging. There is some flexibility with the exact parameterisation; however the method herein used two Thomsen's anisotropic parameters (**?**), ϵ and δ, as well as two angular fields, ϕ and θ, describing dip and azimuth. These are each represented on the same gridded volume as the velocity field, resulting in significant additional necessary memory allocation. In addition to the memory required for allocating the Earth models, more wavefields must be allocated to accurately track these waves, as well as a more intense computational kernel.

When compared to acoustic propagation, TTI uses roughly four times the memory, and is overall around five times slower. This will elaborated upon at the end of Chapter 6. A propagation engine similar to those proposed in **?** and **?** was used. Such methods have been demonstrated to work on migrating field data using RTM

by ?.

Secondly, these data had been processed into down-going receiver gathers, which is typical for OBN imaging (?). This approach uses the first sea-surface related multiple for imaging, since this provides a significant increase in aperture for imaging, with no reduction in signal (since the sea surface is almost a perfect reflector) (?). A schematic detailing the difference between upgoing and downgoing signals for OBN acquisition can be seen in Figure 1. For practical imaging, this is simulated by doubling the water column above the model, and using the sea surface as a mirror - placing the source in this new layer (?). This approach correctly simulates the down-going wavefield, without any up-going events, and is shown in Figure 2.

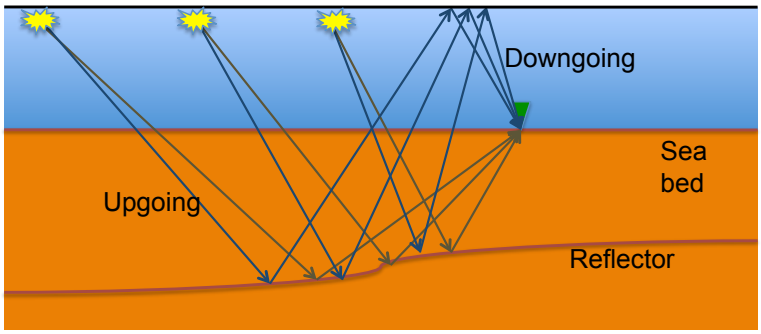

Figure 1: A diagram of upgoing and downgoing rays for OBN acquisition. [**NR**]

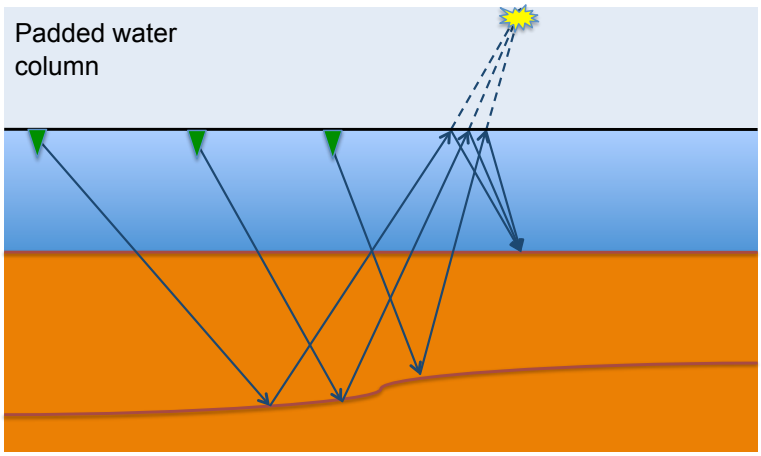

Figure 2: A diagram of how only downgoing rays can be simulated, and the principle of reciprocity. [**NR**]

TTI IMAGES

Figure 3 shows a rotated section of the image produced using TTI RTM on these 103 down-going receiver gathers. The inline aperture (in terms of source positioning) was

greater than the crossline, and this is noticeable. Several salt bodies are identifiable, with well resolved edges, and a variety of reflectors have also been imaged. These events align well in both depth and lateral positioning with a provided reference image. Figure 5 then shows this section after Automatic Gain Control (AGC) has been applied. This is a useful tool on occasion, since it uses a rolling window to artifically boost energy in poorly illuminated areas, and this demonstrates that there are coherent reflectors throughout the entire model. Although there is a significant quantity of imaging induced noise.

Next, Figure 4 shows this same section after five iterations of linearized inversion. The inversion result after AGC is also shown, in Figure 6. There are numerous improvements, but the most pronounced benefits are seen around the salt bodies. The edges and bottoms of these salt bodies are very sharply resolved, with subsalt reflectors becoming more coherent and higher in amplitude. Many contemporary imaging targets are sub-salt, and so a procedure which can improve sub-salt resolution is oft sought after.

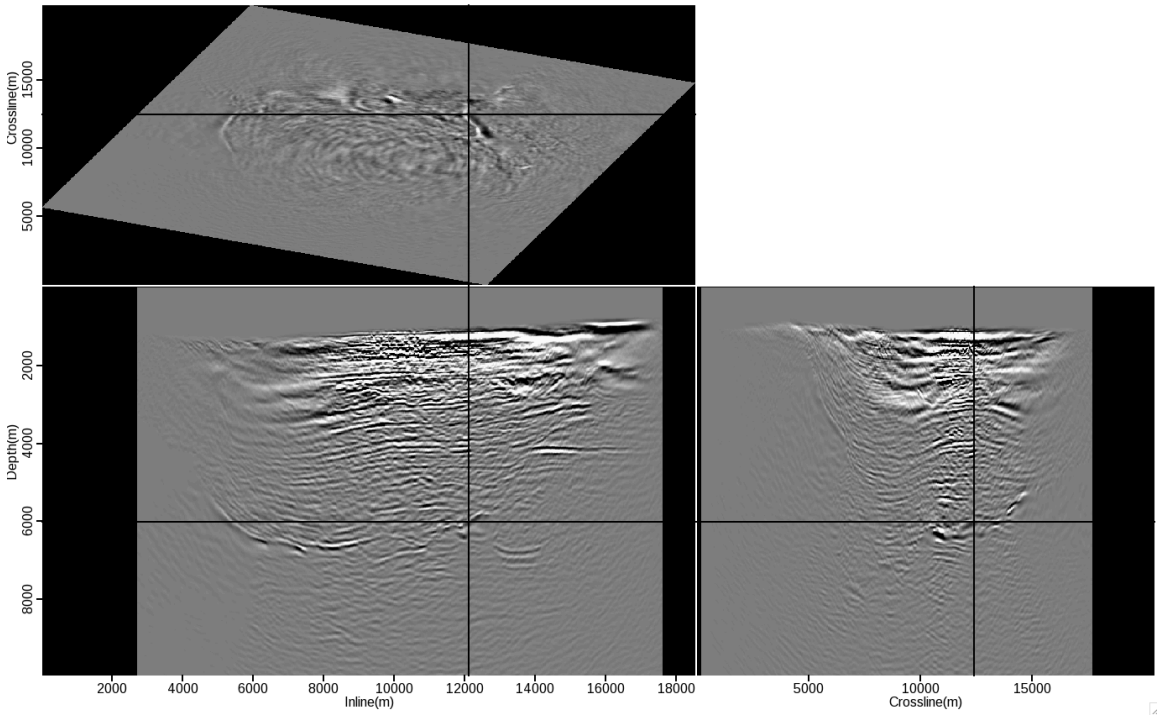

Figure 3: A rotated section of the RTM image, computed from the 103 OBNs. [**NR**]

Other improvements are the general balancing of reflector amplitudes with depth, improved overall coherency of events, higher wavenumber boundaries, and a reduction in imaging related artifacts. It should also be noted that the inversion does struggle in some areas - particularly shallow sediments away from the source lines along the inline direction. This is due in part to the limited aperture in these directions, and due to salt-related refraction events, incorrectly included during imaging.

Nonetheless, given a very large, undersampled model and a relatively sparse set of

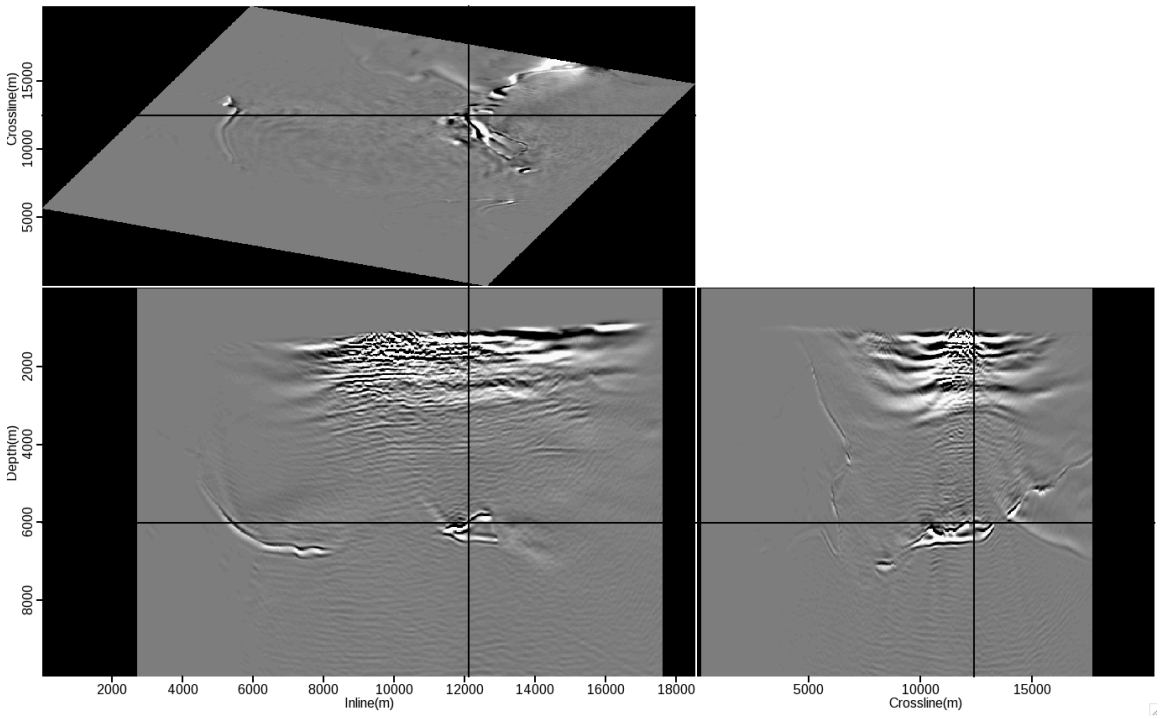

Figure 4: A 3D image at the same coordinates as Figure 3, after five iterations of LSRTM. [**NR**]

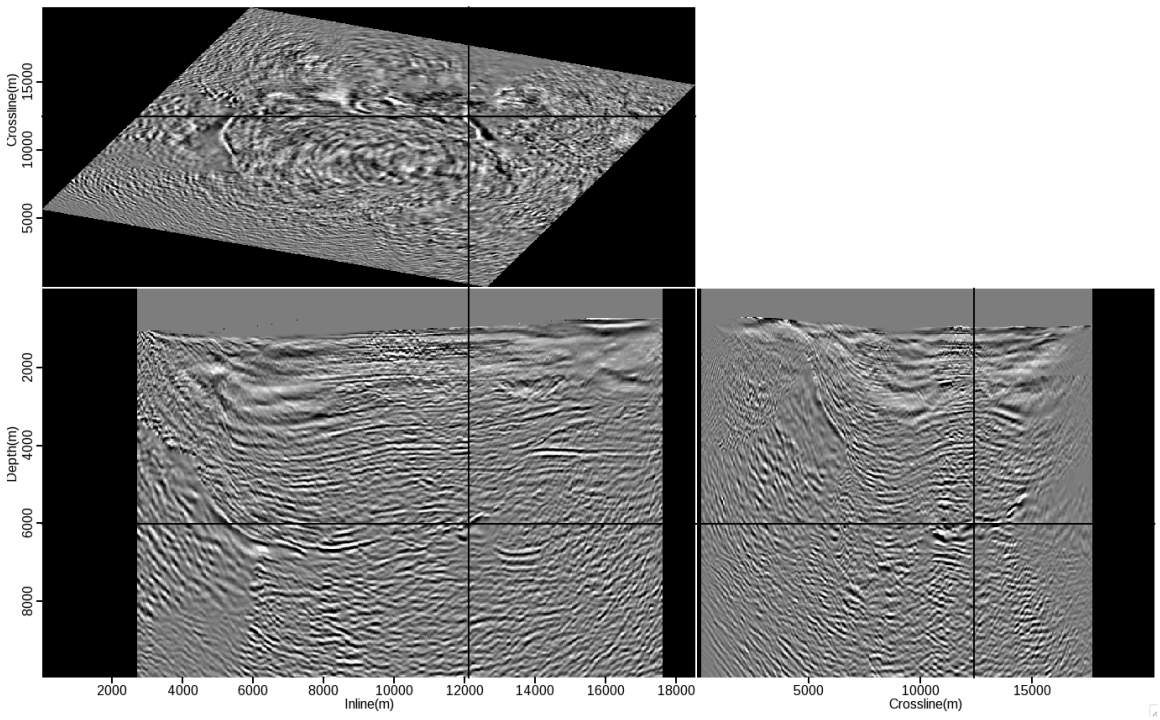

Figure 5: The same result as Figure 3, with AGC applied. [**NR**]

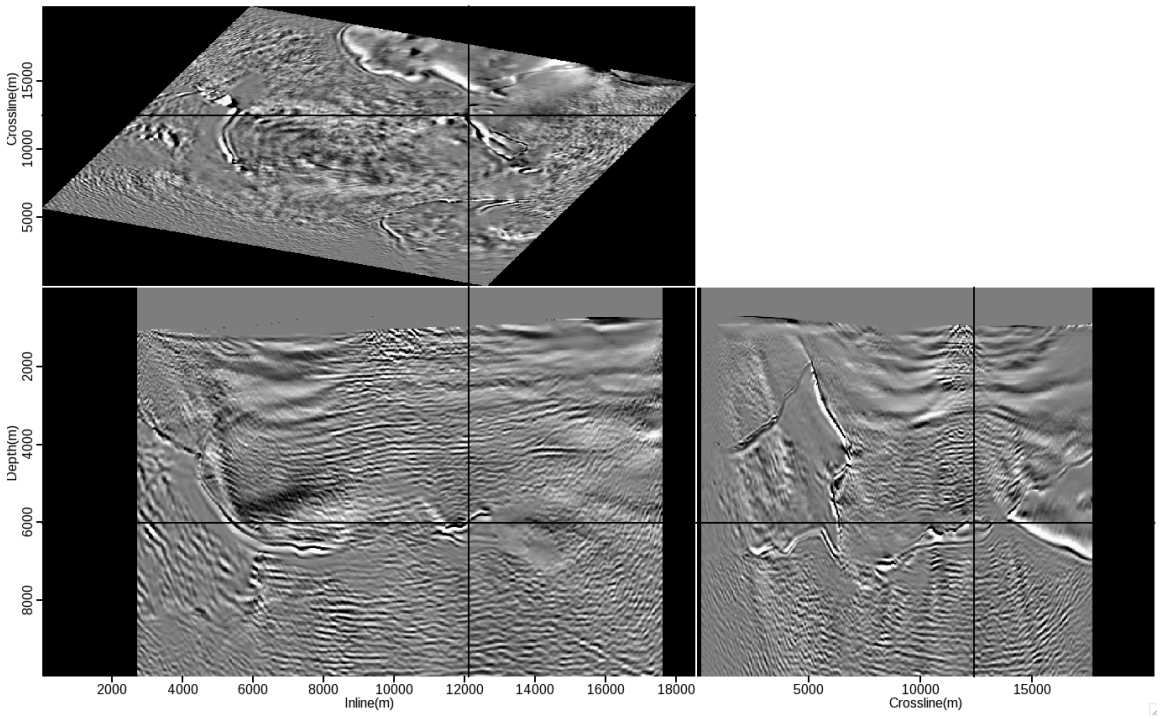

Figure 6: The same result as Figure 4, with AGC applied. [**NR**]

receivers, the improvements of inversion over adjoint imaging are very encouraging.

SOURCE SEPARATION

Simultaneous source shooting can be simply simulated with an OBN dataset, because the receivers are fixed and feature the same (or at least very similar) shooting pattern. Consequently, receiver gathers can be shifted and summed together, due to the linear superposition of these wavefields, to simulate blended acquisition. It is useful that we also have a conventionally imaged result, since we can image these data after separation and then provide a comparison between results.

The same 103 receivers migrated to create these images were combined into random subgroups of five shots, which were then delayed and summed together, with the delay times recorded. Figure 7 shows five such gathers combined, and then Figure 8 shows a windowed shot record from this continuous gathers. These subgroups were used to conserve some I/O cost (these receiver gathers are each 8 Gbytes in size), since reading very large time records can be arduous, but this does not invalidate the simulating of blended acquisition.

The same approach as Chapter 4 was used, which the operator Γ was used to appropriately window the shot of interest from the continuous recording, and image each of these separately. The separation approach used an extremely smoothed and

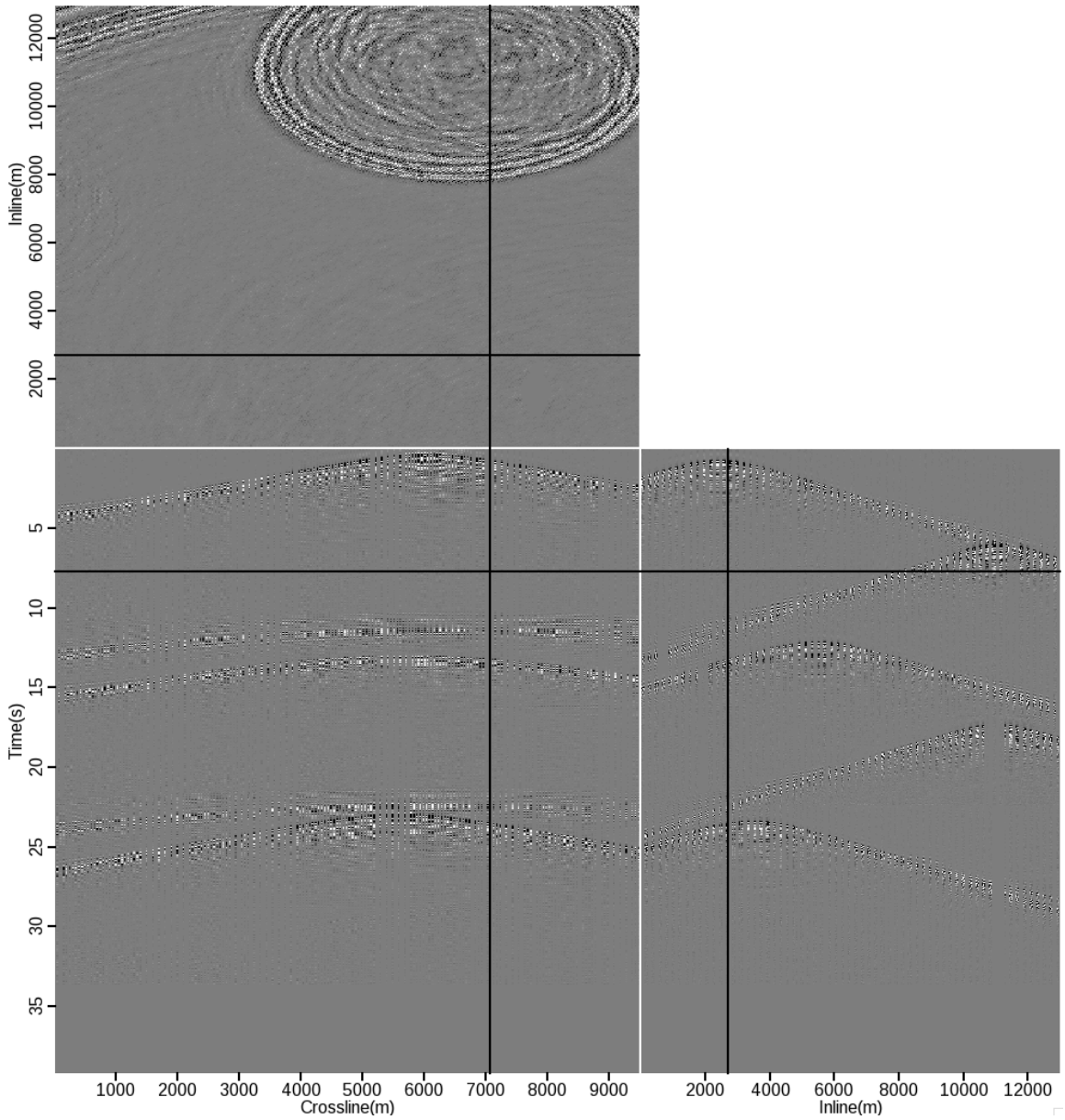

Figure 7: An example receiver gather after five OBNs are blended together. [**NR**]

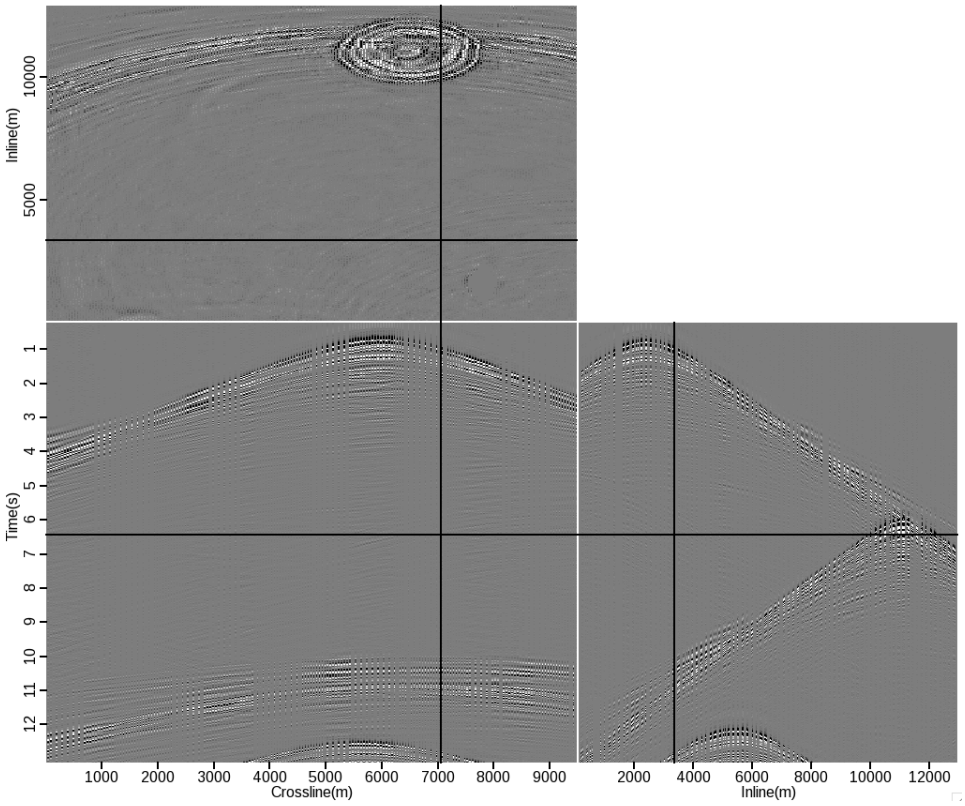

Figure 8: An example input receiver gather for the separation engine, which is a section of Figure 7 after Γ has been applied. [**NR**]

slightly scaled version of the velocity model, and an isotropic, acoustic propagation kernel. Both of these attributes create a sufficiently inaccurate Earth description to test separation. The previous chapter simply smoothed and scaled the velocity, in this case the lack of additional TTI parameters will create further positioning errors. Separation was also performed using the correct velocity model, albeit with an isotropic, unextended separation engine. For both of these separations, ten iterations were used.

Extended imaging was applied in the inline direction, since this featured the densest sampling and the steepest dips. Twenty-five offsets were acquired in total, resulting in 625m of subsurface offsets imaged. This was done using a set of GPUs with a combined memory of about 52 Gbytes. For reasonable runtimes (same order of magnitude as TTI imaging), the entire image must be allocated on the set of GPUs, as such a smaller area of the velocity model was used. The velocity was reduced to a cube of 400 Mbytes, selected by windowing around source positions, all 103 receivers were still used. Tests which offloaded the imaging to allow for more offsets to be acquired slowed the run time by a factor of thirty.

Figure 9 and Figure 10 show some inline image panels, windowed from the 4D image, with subsurface offset panels. Both image panels exhibit some imaging noise, since these are isotropic migrations of anisotropic data, and for the same reason neither panel is tightly focused at zero-subsurface-offset. However, Figure 10 is more loosely focused, and has energy spread over a wider range of subsurface offsets than Figure 9. It also shows some energy focused at non-zero subsurface offset. The zero-offset image from the correct velocity model result, and the full-offset image from the incorrect velocity model result, will now be used to attempt extended forward modeling.

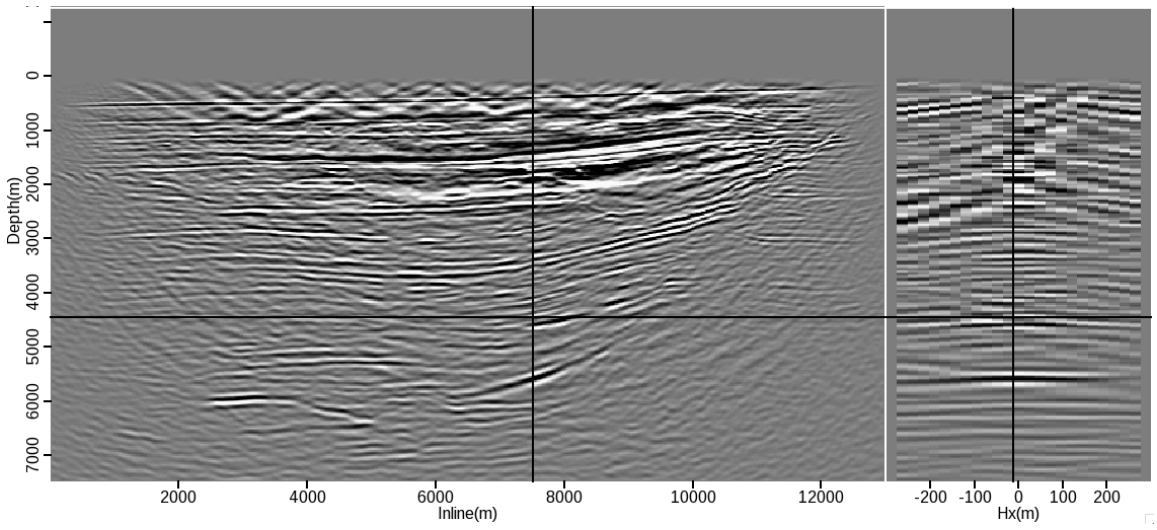

Figure 9: Isotropic, extended migration of these blended data using the correct velocity model. [**NR**]

An input receiver gather, a gather reconstructed with the correct velocity, and a

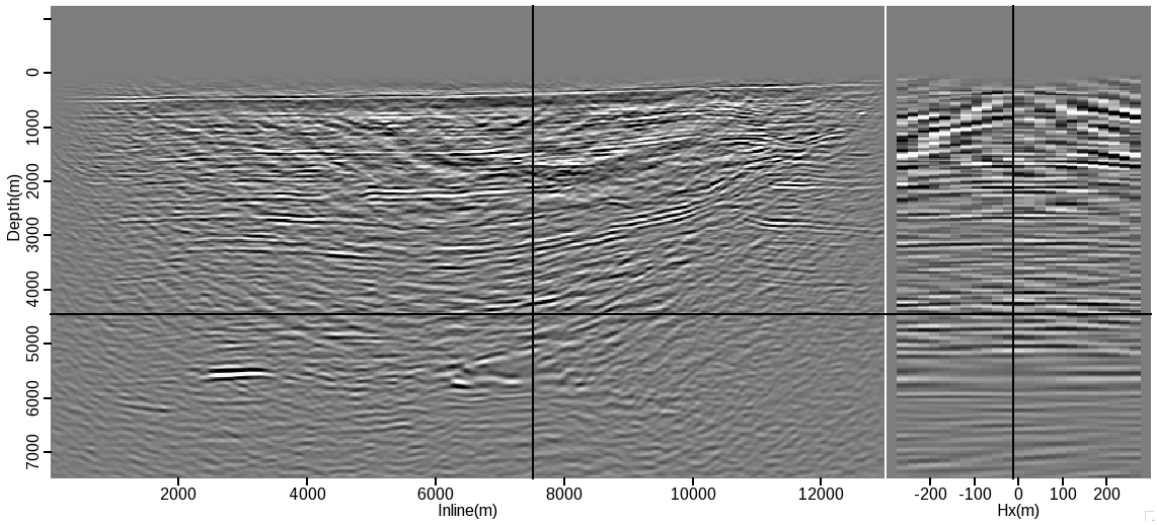

Figure 10: Isotropic, extended migration of these blended data using an incorrect velocity model. [**NR**]

gather reconstructed with the incorrect velocity, are shown in Figre 11; the location selected was in the middle of the domain. Whilst the kinematics are largely present in all three panels, there is some steeply dipping noise at large offsets present in the two reconstructed panels. Since this noise is present in both of the reconstructions, it is not due to extended Born modeling artifacts, which were observed in some of the synthetic tests. It is most likely due to these aforementioned image artifacts, induced from refractions. The salt bodies in these data often cause high velocity refractions, which can easily extend beyond reflection arrivals at large offsets. The limited crossline coverage, in terms of receiver density, means that some of this refraction noise will not stack out effectively in this dimension. This is an interesting phenomenon due to the geometry in question - blended energy stacks out easily, since it is random between shots, and randomly separated in time. Refraction noise, however, is harder to stack out without a variety of crossline receiver positions (these refractions also caused problems for LSRTM, above). Panels which include the recovered corssline data show this more clearly, and can be observed in Figure 12, Figure 13 and Figure **??**. Nonetheless, key reflection events can be mapped in all three panels, and the results of migrating these data show that the separation has preserved reflector information.

For a baseline comparison, these conventional data (unblended receiver gathers) were imaged over this smaller domain, and this baseline image can be seen in Figure 15. The image created using the data reconstructed using the accurate velocity can be seen in Figure 16, and the image created using the data with the incorrect velocity is shown in Figure 17. These are all TTI migrations of these respective datasets, illustrating the best possible image, given the input data.

These images are all directly comparable, and the vast majority of reflectors, contrasts and structures can be seen in all three. Expectedly, the wavenumber content in

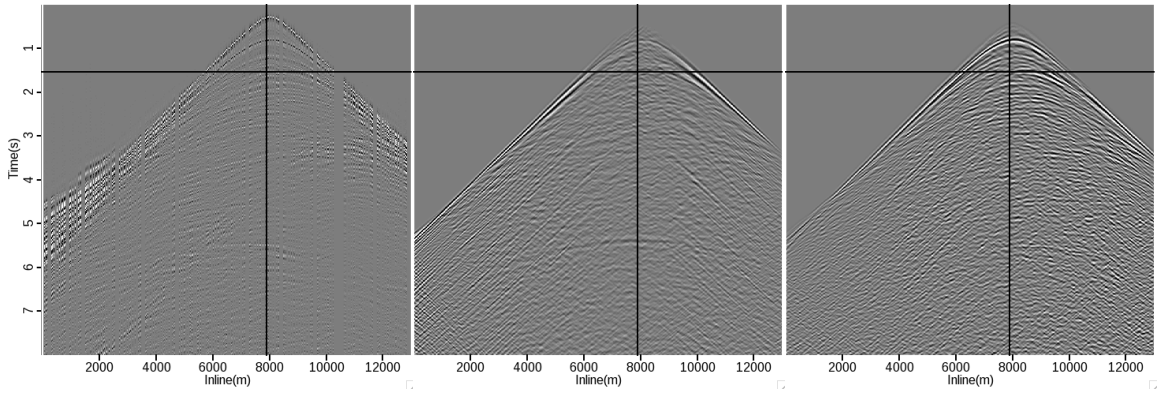

Figure 11: From left to right: an (unblended) receiver gather, the reconstructed gather using extended image space separation and an incorrect velocity model and the reconstructed gather using zero-offset, isotropic image space separation. [**NR**]

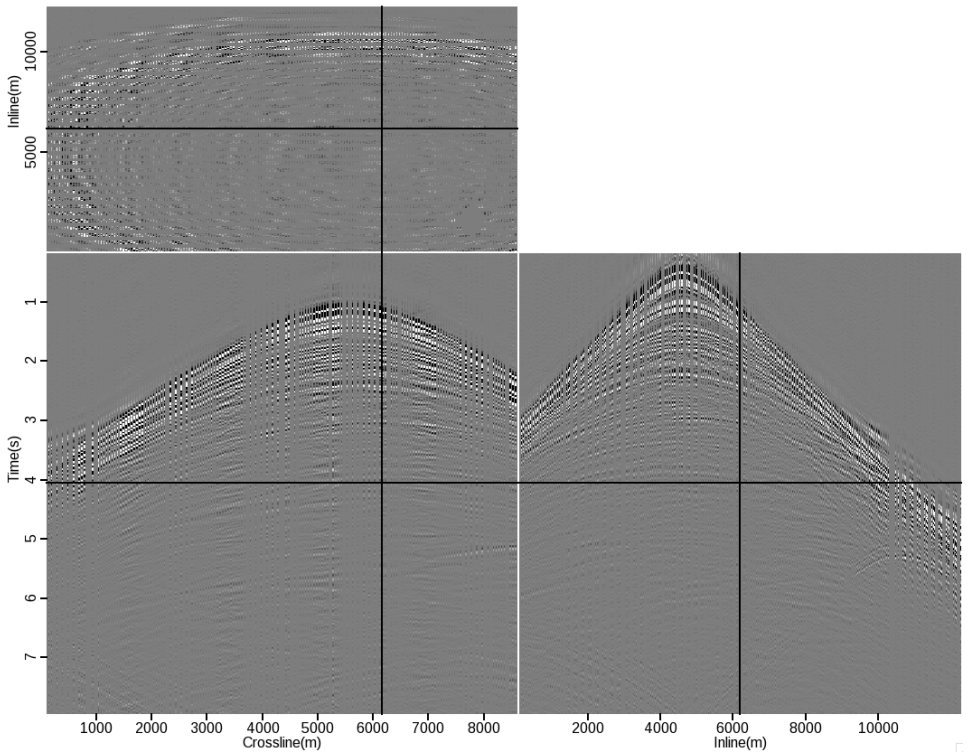

Figure 12: A raw, unblended receiver gather. [**NR**]

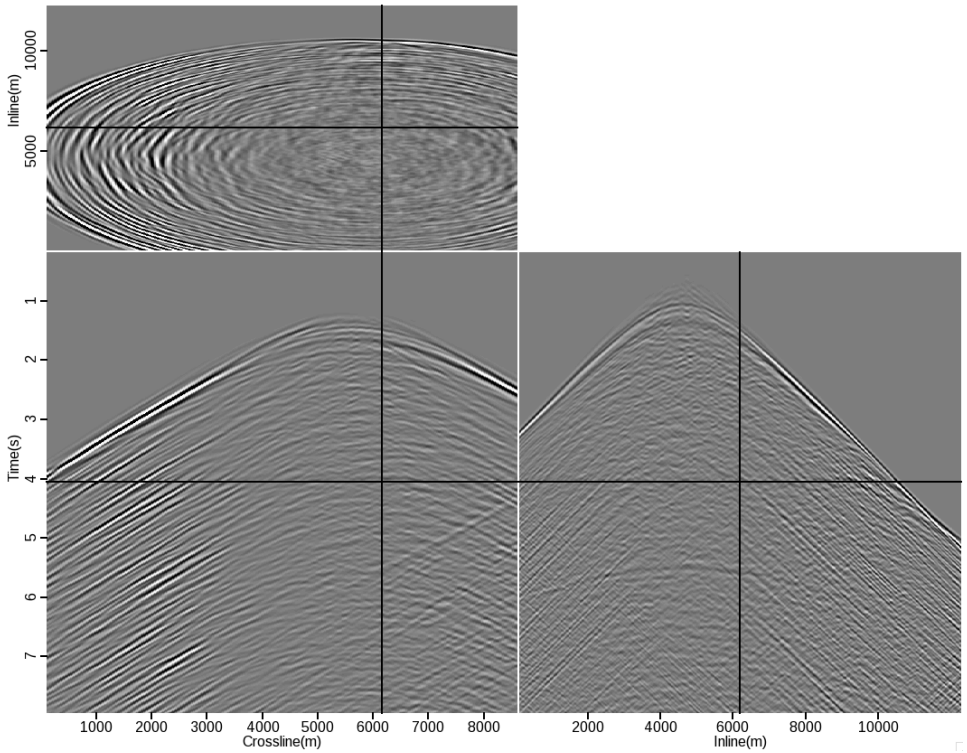

Figure 13: A receiver gather after extended unblending. [**NR**]

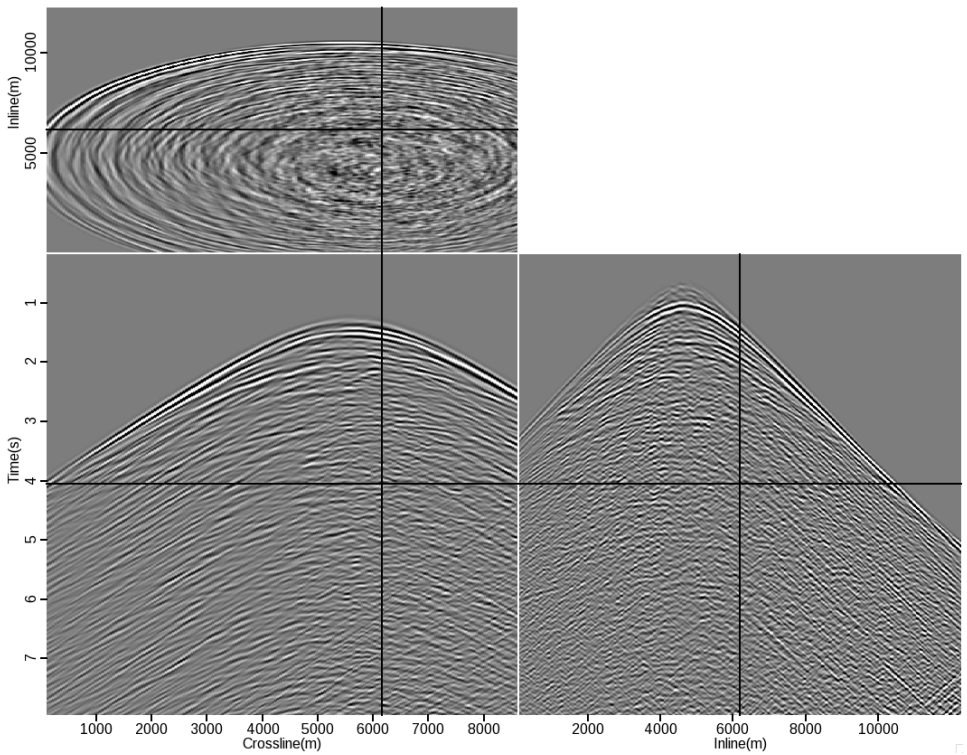

Figure 14: A receiver gather after unextended, isotropic unblending. [**NR**]

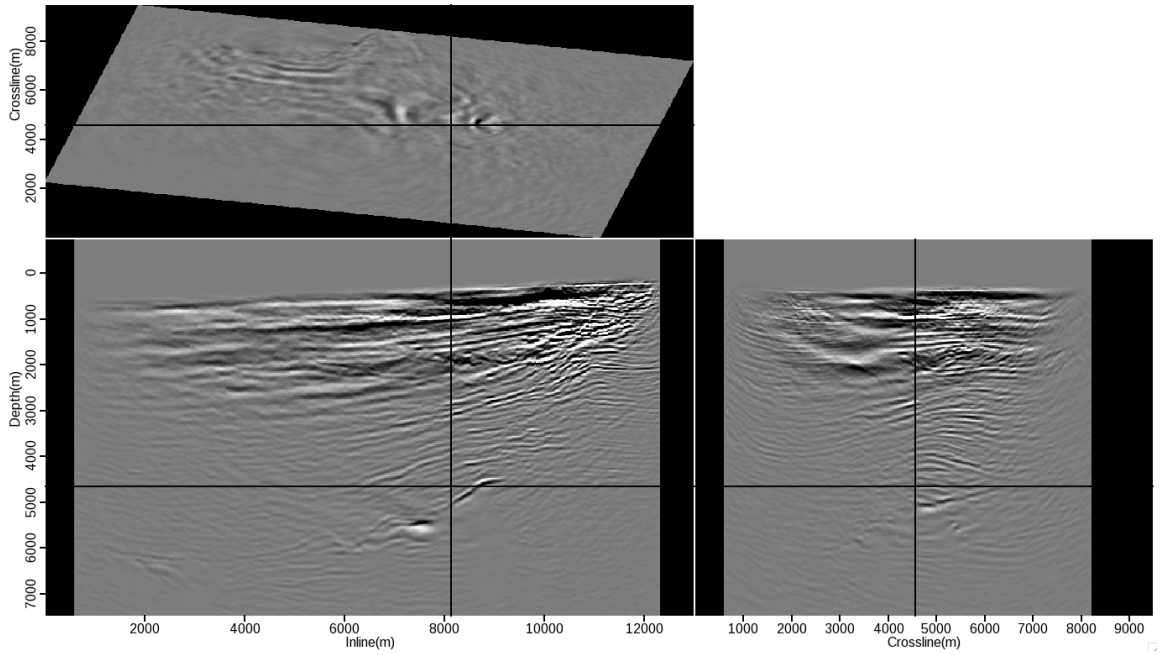

Figure 15: TTI migration of the input data before blending, for a baseline comparison. [**NR**]

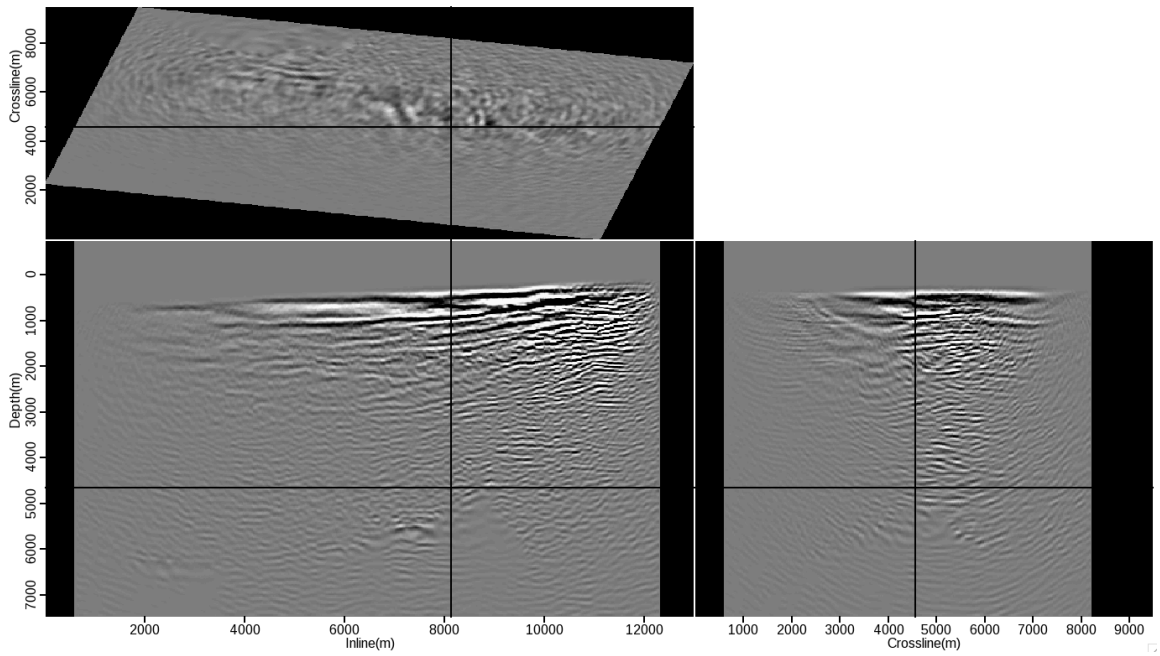

Figure 16: TTI migration of the reconstructed data after 10 iterations of zero-subsurface-offset, isotropic deblending. [**NR**]

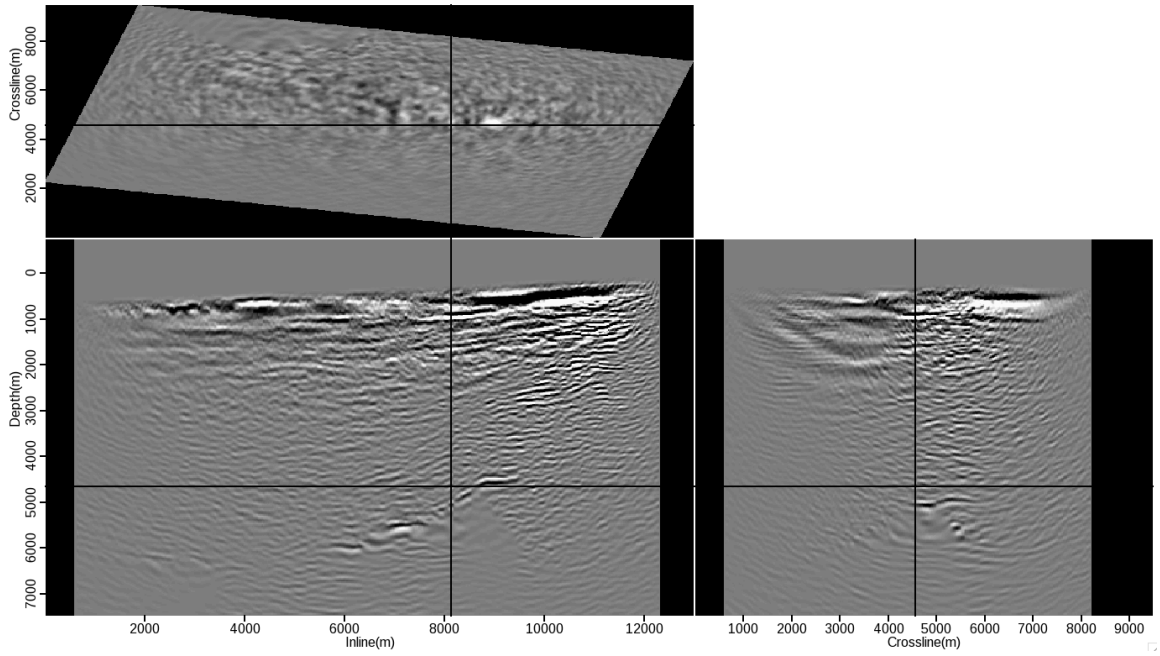

Figure 17: TTI migration of the reconcstructed data after 10 iterations of extended, istropic deblending with a rough velocity model. [**NR**]

the reconstructed panels is a little lower, and the images obtained from the separated data are not quite as well resolved. An series of inlines, for ease of comparison, is shown in Figure 18. For unextended separation, it appears that some information around the salt bodies has been lost, from the subsurface offset panels shown above, this is not entirely surprising. Anisotropic parameters, especially ϕ, are often of higher value around salt bodies - thus, positioning errors are to be expected, and the lack of subsurface offset extension may cause some loss of signal in the image space. These salt edges are better resolved in the image from extended deblending, however this image has a few other imperfections. There is some loss of continuity in the sediments above the salt, and the wavenumber content is lower.

Some of this noise, and continuity disruption, stems from an implementation limitation - only one axis was extended during initial migration. For this dataset, the choice of axis was obvious, since the source sampling along the inline direction was much more consistent and dense. Despite the limited dip content of the crossline direction, it is probable some information was lost at this point. By extending the migration in both x and y, energy would not be lost in this manner. Another choice would be to use time lag imaging, as this would capture unfocused arrivals in any spatial direction. However, the restraints of the computers and the input data size meant that multiple spatial lags, or time lags, would be close to unfeasible.

Despite only extending one axis, it is encouraging that dipping reflectors at the edge of the crossline panels are still imaged in all three cases. This helps to confirm that only marginal information was lost in the extended deblending, and further

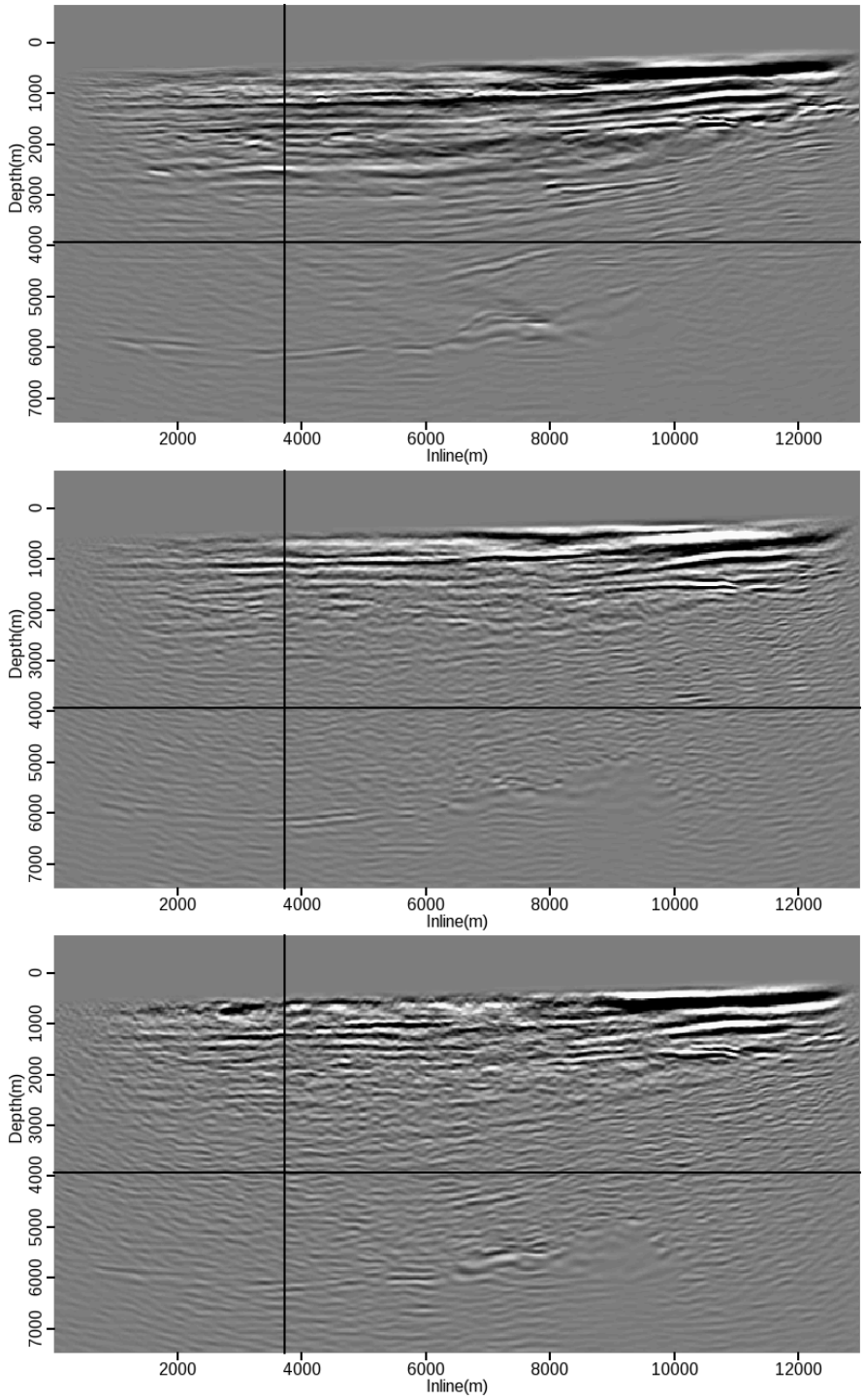

Figure 18: An inline comparison of the images shown in Figure 15, Figure 16 and Figure 17. [**NR**]

iterations would improve the results.

As discussed in the previous chapter, image-space separation can be augmented into a model-building and imaging process. In this context, then these results are even more encouraging. All output images well represent the geology, structure and amplitude character of the subsurface, and as the model improves, then this representation will become stronger. Furthermore, all would act as powerful starting models for any sort of subsequent linearized inversion. If this scheme were to be combined with, say, migration velocity analysis, then an effective positive feedback loop could be created. The extended images are already created, which can be used to provide a velocity model update. This updated model could then be used to improve the separation fidelity, and the process repeated.

CONCLUSIONS

These results demonstrate that extended image space blended inversion is effective for shot separation. Given a blended input dataset, this technique was effective in separating these shots into separated gathers using both an accurate and an inaccurate velocity model. Furthermore, the separation engine was isotropic, and the velocity model was built under the assumption of TTI anisotropy, so both attempts will exhibit inaccuracies in the migration.

Imaging these separated datasets was successful and representative, however, both results suffered from a reduction in frequency and a variety of implementation artifacts.

ACKNOWLEDGMENTS

Special thanks to Scott Morton, of Hess Corporation, for making all the work in this chapter possible. Scott helped with data access, concepts, interpretation and practical implementation discussions. Special thanks also to Wayne Lee and Faqi Lui, of Hess Corporation, for their assistance in harnessing the computational system, and analysing results, respectively.